JACS
JOURNAL OF THE AMERICAN CHEMICAL SOCIETY
pubs.acs.org/JACS
Article

Atomically Dispersed Catalytic Platinum Anti-Substitutions in Molybdenum Ditelluride

Jun Zhao,[†] Xiaocang Han,[†] Junxian Li,[†] Ziyi Han, and Xiaoxu Zhao*

Cite This: J. Am. Chem. Soc. 2025, 147, 9825−9835
Read Online
ACCESS | Metrics & More | Article Recommendations | Supporting Information

ABSTRACT: Atomic defects, e.g., vacancies, substitutions, and dopants, play crucial roles in determining the functionalities of two-dimensional (2D) materials, including spin glass, single-photon emitters, and energy storage and conversion, due to the introduction of abnormal charge states and noncentrosymmetric distortion. In particular, anti-substitutions are regarded as promising topological defect types, in which substitution occurs at opposite charge sites, fundamentally modifying the atomic and electronic structures of pristine lattices. However, the fabrication of large-scale anti-substitutions remains challenging due to high formation energies and complex reaction paths. Here, we propose an approach for synthesizing atomically dispersed Pt anti-substitutions in defective 1T′-$MoTe_2$ using the electrochemical exfoliation-assisted leaching−redeposition (EELR) method. Atomic-resolution scanning transmission electron microscopy (STEM) imaging reveals that Pt atoms substitute Te sites, forming unconventional Mo−Pt bonds. A rich variety of Pt anti-substitution configurations and Pt anti-substitutions coupling with Te vacancies have been fabricated by controlled electrochemical conditions. Density functional theory (DFT) calculations suggest that Pt atoms preferentially occupy the Te vacancy sites coupled with neighboring Te vacancies, stabilizing the anti-substitution configurations. The coupled Pt−Te defect complexes exhibit excellent hydrogen evolution reaction, with an overpotential of only 12.9 mV because the paired defect complexes cause charge redistribution and regulate the d-band center of the active sites as suggested by DFT. These findings introduce an effective approach for engineering atomically dispersed anti-substitutions in 2D materials, presenting new opportunities for the precise design of atomic features with targeted functionalities in catalytic and other advanced applications.

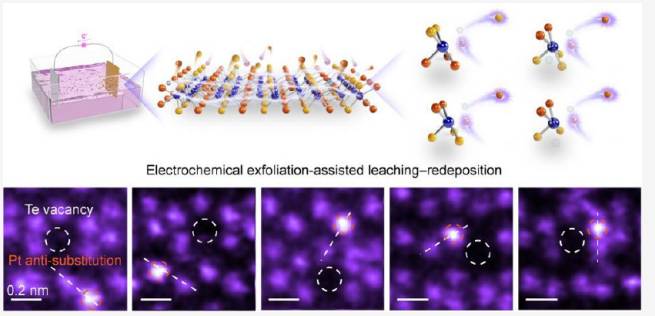

INTRODUCTION

Atomic defects are inherent and unavoidable features of crystal materials, driven by the second law of thermodynamics.[1] The introduction of these defects often initiates structural rearrangements and charge redistributions, which, in turn, significantly influence orbital hybridization and the electronic structure of materials.[2−5] The distinct three-atom-thick architecture of monolayer transition metal dichalcogenides (TMDs) provides an optimal platform for engineering a range of atomic defects, such as vacancies, antisites, substitutions, and adatoms.[6−8] Defect engineering in TMDs has been extensively explored, demonstrating its power in modulating optical,[9,10] electrical,[11,12] magnetic,[13,14] and mechanical[15,16] properties to unlock new functionalities, which holds considerable promise for applications in nanomagnetic systems,[17] novel exciton emissions,[18] defect-based qubits,[19] flexible electronics,[20] catalytic chemistry,[21] etc.

The diversity of defect configurations in TMD monolayers offers a broad spectrum of precisely tunable physiochemical properties. For instance, prevalent anion vacancies in the as-grown TMD samples, are well recognized for their crucial role in shaping electronic behavior, particularly by introducing deep in-gap defect levels.[22−24] In antisite Mo_s defects, a local magnetic moment of 2 μB has been predicted, attributed to the strong orbital hybridization between the center Mo atom and neighboring Mo and S atoms.[25] Additionally, neutral anion-antisite defects (W_s and W_{Se}) in 1H-phase group-VI TMDs reveal promising potential as defect-spin qubits, capable of hosting stable triplet ground states.[19] Substitutions doping in monolayer TMDs are comparably intriguing, as oxygen-incorporated V_s sites in monolayer MoS_2 can effectively passivate sulfur vacancies, suppress the formation of donor states, and thereby lower the electrical contact resistance.[23] Besides, substituting 50% of Mo with Re in MoS_2 induces a phase transition, resulting in wider channels between cation chains and offering supreme active sites for catalysis.[26]

Received: January 1, 2025
Revised: February 19, 2025
Accepted: February 21, 2025
Published: March 5, 2025

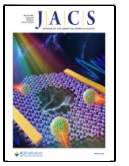

https://doi.org/10.1021/jacs.5c00033
J. Am. Chem. Soc. 2025, 147, 9825−9835

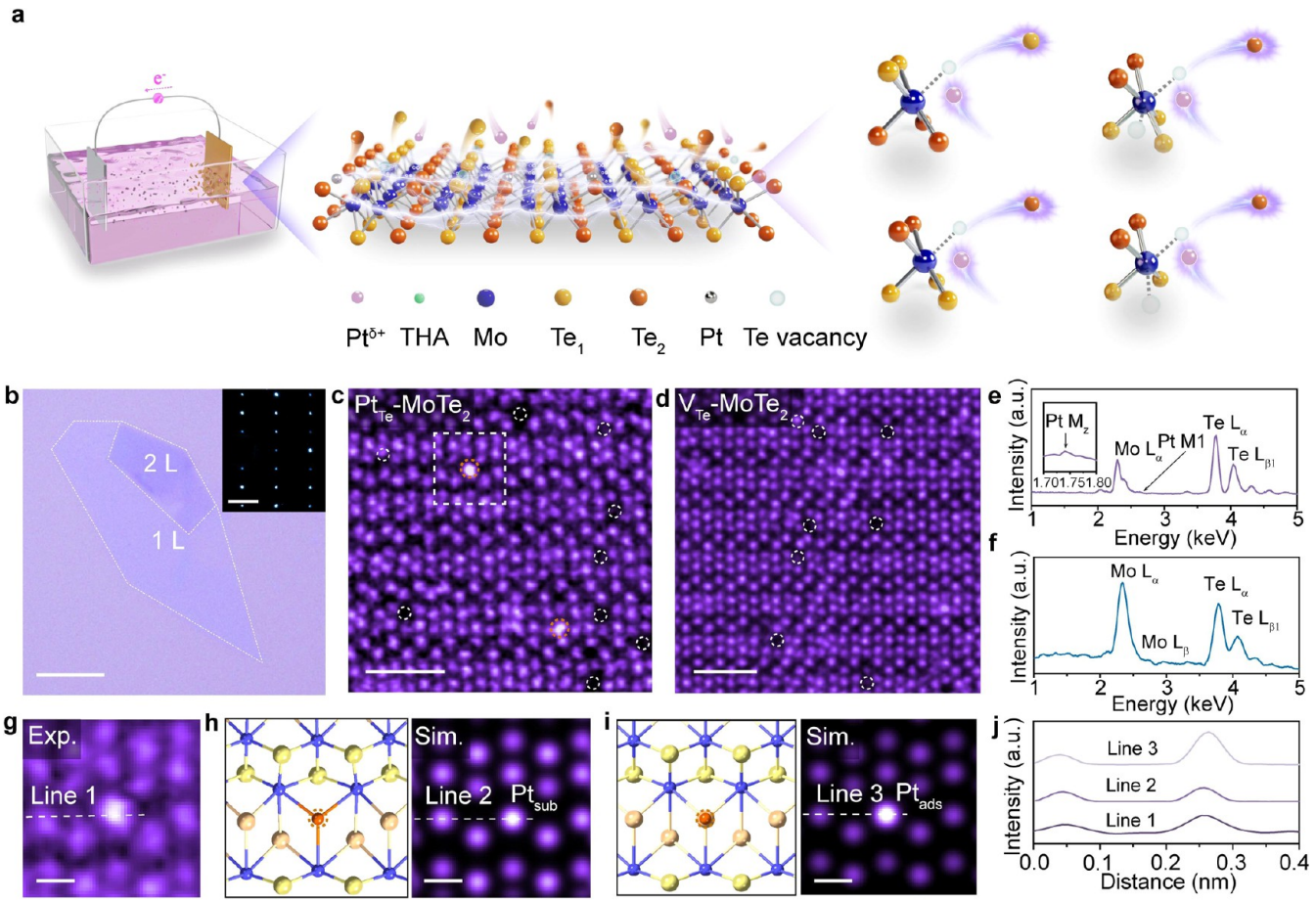

Figure 1. Fabrication of Pt_{Te} anti-substitution in monolayer 1T′-$MoTe_2$. (a) Schematic illustration depicting the growth of Pt_{Te} anti-substitution in 1T′-$MoTe_2$ monolayer via the electrochemical exfoliation-induced leaching and redeposition method. (b) Optical microscopy and selected area electron diffraction (SAED) images of exfoliated 1T′-$MoTe_2$ flakes. (c, d) Annular dark-field scanning transmission electron microscopy (ADF-STEM) image showing the (c) Pt atoms and Te vacancies and (d) Te vacancies in 1T′-$MoTe_2$ using Pt foil or graphite rod as the anode, respectively. (e, f) Corresponding energy-dispersive X-ray spectroscopy (EDS) of Pt_{Te}-$MoTe_2$ (e) and V_{Te}-$MoTe_2$ (f). (g) ADF-STEM image of white box region from (c) showing the configuration of Pt_{Te} anti-substitution. Atomic models and corresponding simulated images of (h) Pt substituting the Te site, and (i) Pt adsorbing on the Te site. (j) Intensity line profiles of Te and Pt sites in (g–i). Scale bars: (b) 5 μm, (c) 1 nm, (d) 1 nm, (g–i) 0.2 nm.

Controlled substitution holds great potential for producing atomic-scale local magnetic moments, reducing electrical contact resistance, and enhancing catalytic activity. However, substitutions are confined to heterovalent and isovalent, where doping occurs at the same type of ionic site.[27−29] Anti-substitution, which is particularly unique due to its potential for novel functionalities,[19] is rare because of the high formation energies of oppositely charged sites,[30] environmental factors, and crystal symmetry constraints.[19,31] Consequently, achieving large-scale, atomic-scale anti-substitution in TMD monolayers remains challenging, and their intriguing functionalities are elusive.

In this work, we synthesized atomically dispersed Pt anti-substitutions by electrochemical exfoliation-assisted leaching−redeposition (EELR) method. Atomic-resolution annular dark-field scanning transmission electron microscopy (ADF-STEM) imaging confirmed that Pt single atoms were kinetically driven to occupy Te vacancy sites, forming anti-substitutions, where considerable Te vacancies were in situ generated during the exfoliation of 1T′-$MoTe_2$. In the sample containing a low density of Te vacancies, five distinct structures of Pt anti-substitution defects were observed. At a lower voltage of −4 V, which produces a higher density of Te vacancies, vacancy complexes containing coupled Te vacancy and Pt anti-substitution emerge. Density functional theory (DFT) calculations indicate that Te vacancies in 1T′-$MoTe_2$ preferentially attracts Pt anti-substitution atoms, releasing energy and stabilizing the defect structure. Electrochemical measurements show that samples containing paired Pt anti-substitutions and Te vacancies exhibit excellent catalytic performance, with an overpotential of only 12.9 mV versus a reversible hydrogen electrode (RHE) at a current density of 10 mA cm^{-2}. First-principles calculations disclose that coupled structures result in charge redistribution, regulate the d-band structure of both Pt and Mo sites, optimize the hydrogen adsorption energy, and ultimately enhance the hydrogen evolution efficiency.

RESULTS AND DISCUSSION

Synthesis and Characterization of Pt Anti-Substitutions in 1T′-$MoTe_2$. Electrochemical exfoliation is a widely utilized method for producing monolayer TMDs,[32] during which chalcogen vacancies are preferentially generated.[33] The vacancies could serve as ideal sites for the incorporation of other groups (or atoms).[34] Leveraging this property, Pt atoms

https://doi.org/10.1021/jacs.5c00033
J. Am. Chem. Soc. 2025, 147, 9825−9835

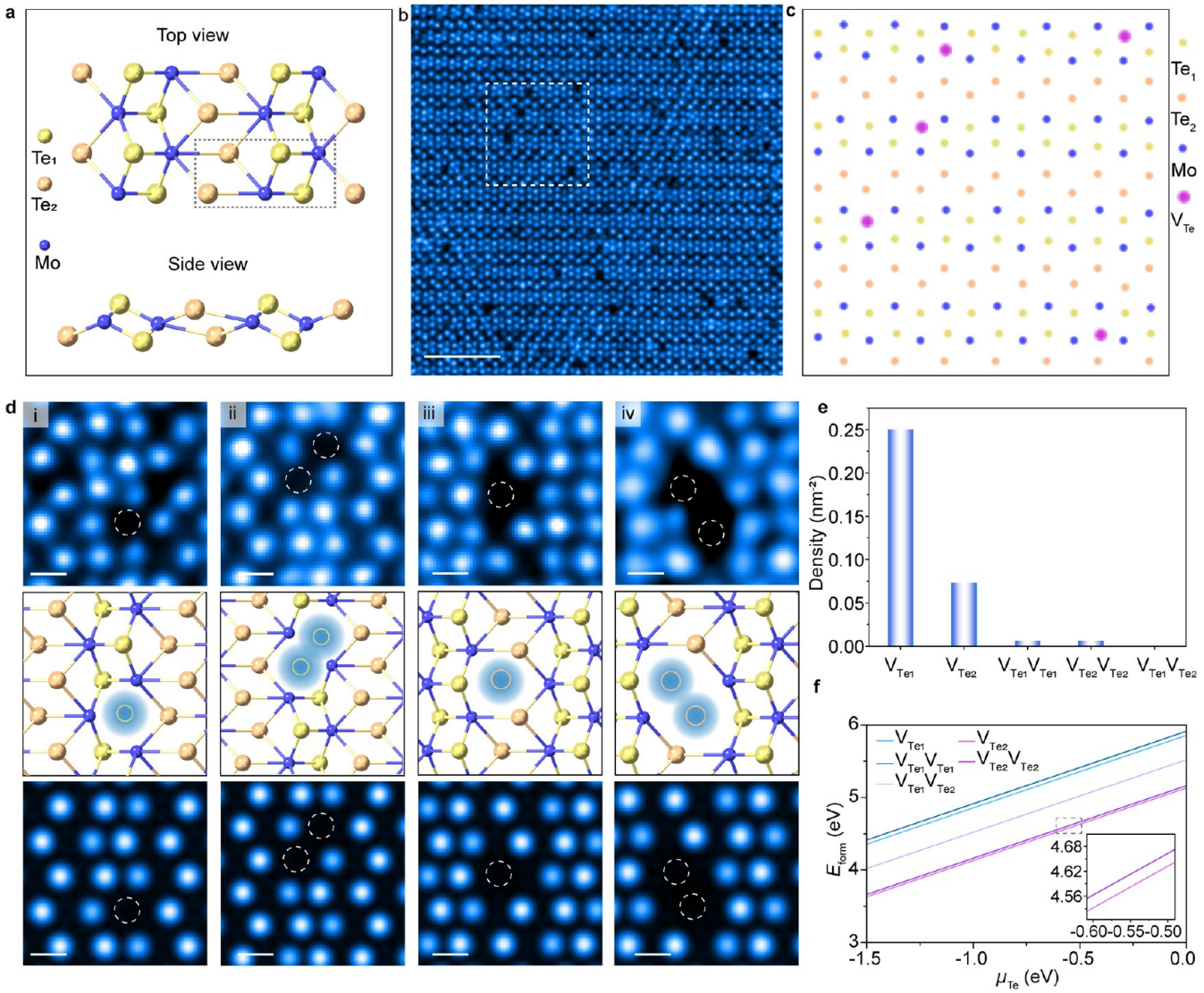

Figure 2. Atomic structures of Te vacancies in 1T′-$MoTe_2$. (a) Atomic models of 1T′-$MoTe_2$. (b) Atomic-resolution annular dark-field STEM (ADF-STEM) image of monolayer 1T′-$MoTe_2$ containing abundant Te vacancies. (c) Schematic atomic model of white box region from (b) revealing the spatial distribution of Te vacancies in monolayer 1T′-$MoTe_2$. Blue balls, Mo atoms; yellow balls, Te_1 atoms; light orange balls, Te_2 atoms; pink balls, single Te vacancy sites (V_{Te}). (d) Zoom-in ADF-STEM images showing a variety of Te vacancy configurations, with the corresponding atomic models and simulated images displayed in the middle and bottom panels, respectively. (e) Statistical counting of four predominant types of Te vacancies. (f) DFT-calculated formation energies of various Te vacancies in monolayer $MoTe_2$ as a function of Te chemical potential. Scale bars: 2 nm in (b), 0.2 nm in (d).

were introduced into the Te vacancy sites in 1T′-$MoTe_2$ during the electrochemical exfoliation process when using a Pt foil as the anode (Figure 1). The Pt atoms originated from Pt foil infiltrated and subsequently deposited into Te vacancy sites, a process termed the electrochemical exfoliation-induced leaching and redeposition method, as depicted in Figure 1a. In the electrochemical exfoliation process, 1T′-$MoTe_2$ bulk crystals are utilized as the cathode, and tetraalkylammonium halides (THA) and acetonitrile are employed as intercalation agents and electrolyte solutions, respectively, facilitating effective ion intercalation and subsequent exfoliation. Under a negative electrochemical potential of −3 V, tetrahexylammonium cations intercalate into the van der Waals (vdW) gaps of bulk 1T′-$MoTe_2$ crystals, leading to interlayer expansion (Supporting Figure 1).[35] Upon gentle sonication, large numbers of monolayer $MoTe_2$ nanosheets were prepared (Figure 1b and Supporting Figure 2).[36] The selected area electron diffraction (SAED) pattern (Figure 1b, inset) confirms that the as-prepared 1T′-$MoTe_2$ nanosheets are single-crystalline.

Atomic-resolution ADF-STEM image (Figure 1c) reveals that the as-exfoliated 1T′-$MoTe_2$ is a monolayer containing a significant number of Te vacancies and atomically dispersed Pt dopants, as further confirmed by the energy-dispersive X-ray spectroscopy (EDS) (Figure 1e). To examine the Pt source during the exfoliation, a graphite rod was used to replace Pt foil as the anode for comparison. As expected we did not find any Pt dopants (Figure 1d,f), and a large number of Te vacancies were detected instead serving as the host for foreign Pt adatoms.[33,37]

To validate the atomic configurations, i.e., either surface absorption or lattice replacement of Pt dopants, the intensities of the Pt atomic blobs in the ADF-STEM images were precisely analyzed (Figure 1g–j). Two doping configurations

https://doi.org/10.1021/jacs.5c00033
J. Am. Chem. Soc. 2025, 147, 9825−9835

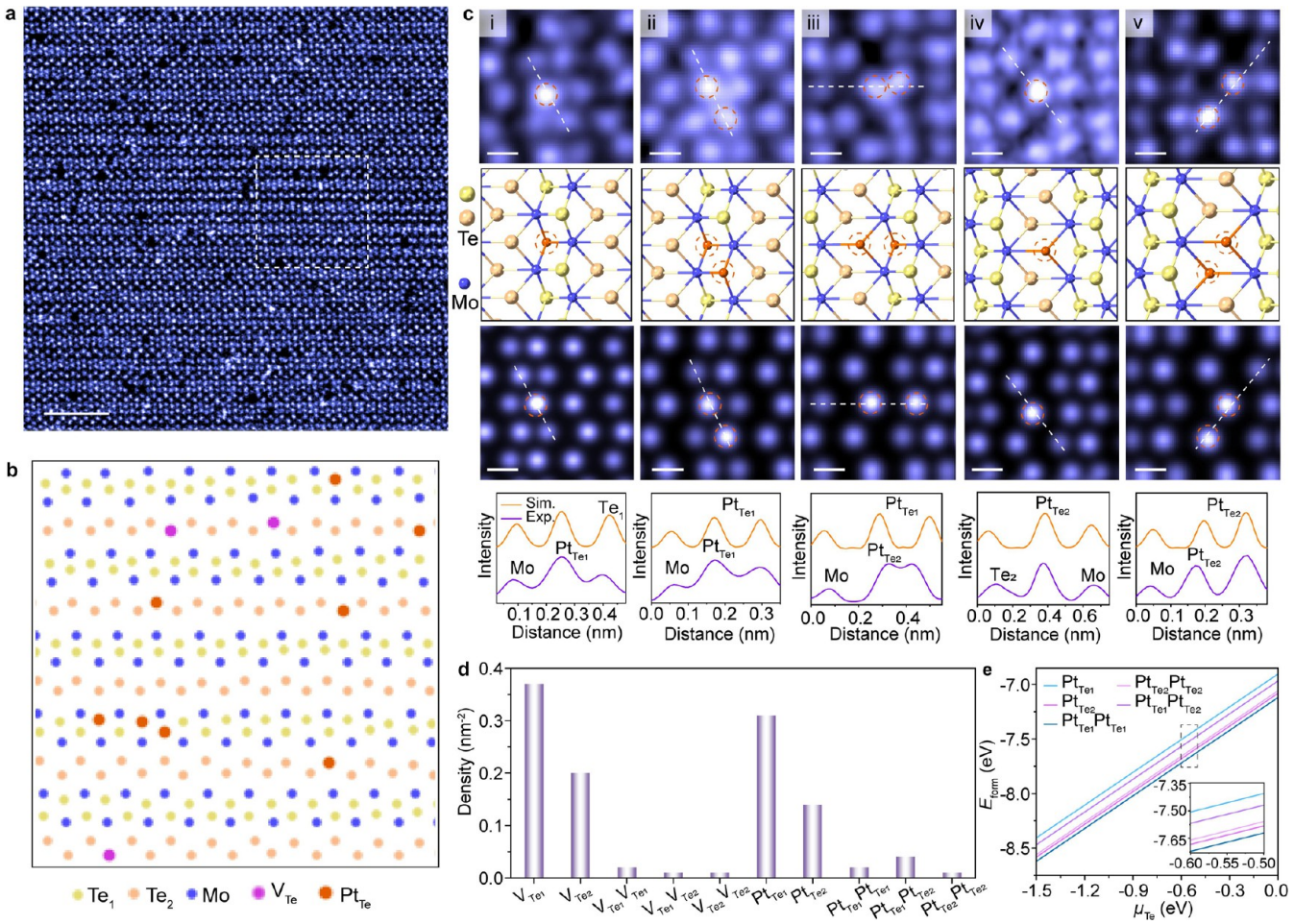

Figure 3. Atomic structures of Pt anti-substitutions in 1T′-$MoTe_2$. (a) Atomic-resolution ADF-STEM image of Pt_{Te}-$MoTe_2$. (b) Schematic atomic model of white box region from (a) illustrating the spatial distribution of Pt anti-substitutions and Te vacancies. Blue balls, Mo atoms; yellow balls, Te_1 atoms; light orange balls, Te_2 atoms; orange balls, Pt_{Te} anti-substitutions; pink balls, Te vacancies. (c) Atomic-resolution ADF-STEM images showing the different anti-substitution structures of (i) Pt_{Te_1}, (ii) $Pt_{Te_1}Pt_{Te_1}$, (iii) $Pt_{Te_1}Pt_{Te_2}$, (iv) Pt_{Te_2}, (v) $Pt_{Te_2}Pt_{Te_2}$, with corresponding atomic models, simulated images, and intensity line profiles displayed in sequence from top to bottom panels, respectively. (d) Statistical counting of a variety of vacancies and anti-substitutions. (e) DFT-calculated formation energies of various anti-substitutions as a function of Te chemical potential. Scale bars: (a) 2 nm, (c) 0.2 nm.

were simulated: Pt substituting for the Te site (Pt_{Te}) and Pt adsorbed on the top of the Te site. It can be seen that the experimental image (Figure 1g) greatly resembles the simulated images derived from the substitution model (Figure 1h) rather than the adsorption model (Figure 1i), as verified by the intensity ratios between Pt and Te atom blob, which reveal 1.3, 1.2, and 3.2, respectively. In addition, we found that Pt atoms are relatively immobile upon the e-beam irradiation, which further suggests the strong interaction between Pt atoms and adjacent atoms. Therefore, we can confirm the creation of Pt_{Te}-$MoTe_2$ anti-substitutions rather than surface absorption by the EELR method.[32]

To systematically examine the atomic structure of Te vacancies in 1T′-$MoTe_2$, we conducted the exfoliation process utilizing a graphite rod, denoted as V_{Te}-$MoTe_2$ (Supporting Figure 3 and Supporting Table 1). Atomic-resolution ADF-STEM image shows that Te could be precisely identified (Figure 2b) based on the *Z*-contrast ADF image. Distorted 1T phase (1T′) in monolayer $MoTe_2$ exhibits unique zigzag chains displaying a 1 × 2 metal dimerization superstructure, which contain two nonequivalent Te sites (Te_1, and Te_2) in one unit cell, marked by yellow and light orange colors, respectively (Figure 2a). Based on a hierarchy framework, i.e., Zernike polynomial (ZP) clustering,[38] specific types of Te vacancies can be efficiently and precisely identified and classified (Figure 2c and Supporting Figures 4 and 5). Four predominant Te vacancies and vacancy complexes are spotted, i.e., V_{Te_1}, V_{Te_2}, $V_{Te_1}V_{Te_1}$, and V_{Te_2}, V_{Te_2} (Figure 2d), as confirmed by the corresponding simulated images (Figure 2d). Statistically, vacancies are prone to occur at the Te_1 site with a density of 0.25 nm^{-2} (Figure 2e). The formation energy of Te vacancies as a function of the Te chemical potential is calculated by DFT (Figure 2f). It can be seen that V_{Te_2} exhibits the lowest formation energy, whereas V_{Te_1} is relatively higher, presumably ascribed to the relatively large space volume of the Te_2 site compared to the Te_1.[39] Despite being energetically less favorable, the actual density of V_{Te_1} surpasses that of V_{Te_2}, implying that the generation of Te vacancies is presumably mediated by a kinetic growth process.

It has been demonstrated that a large number of Te vacancies can be generated during electrochemical exfoliation. To validate whether those vacancies can be in situ occupied by

https://doi.org/10.1021/jacs.5c00033
J. Am. Chem. Soc. 2025, 147, 9825−9835

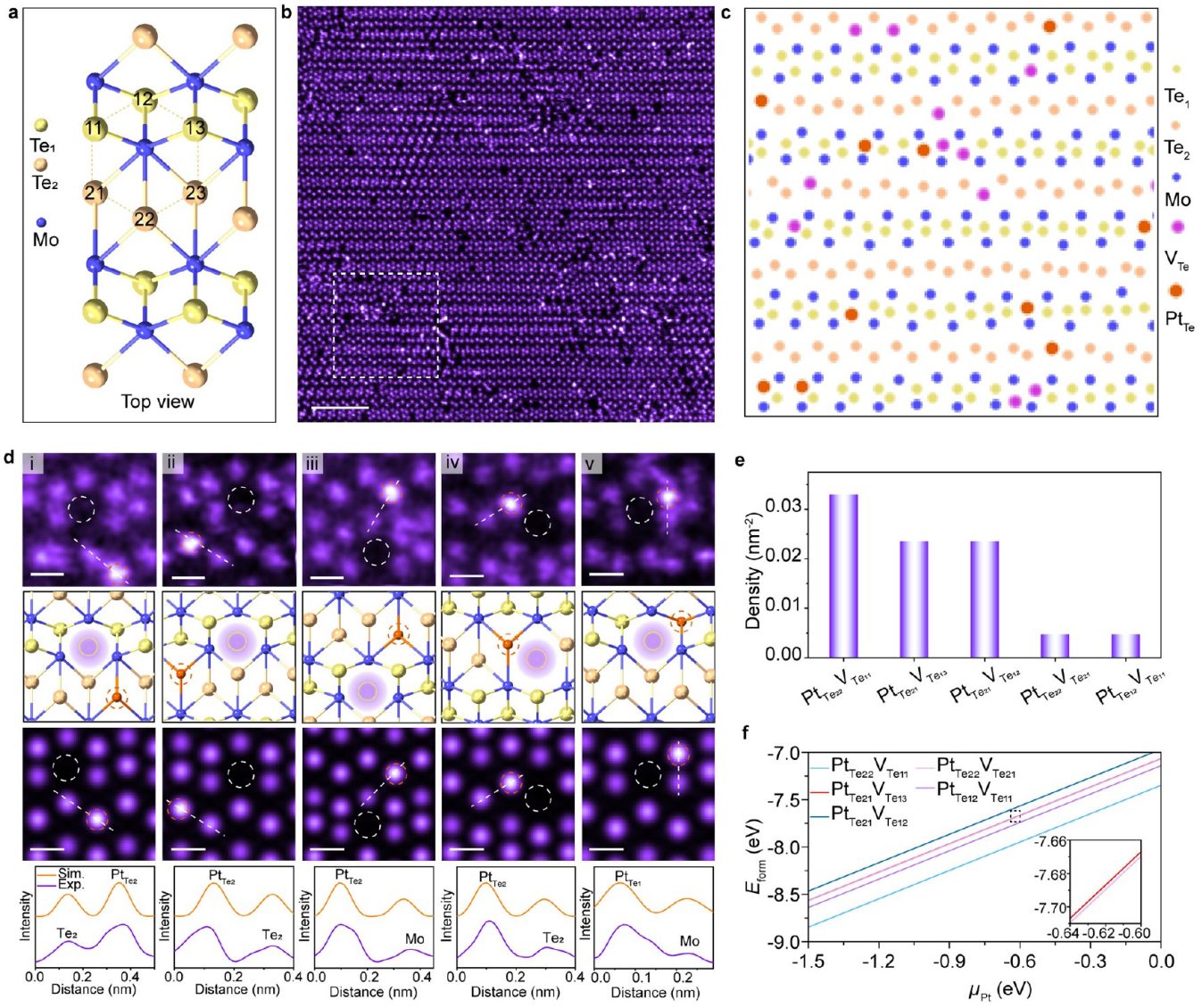

Figure 4. Atomic structures of coupled anti-substitution-vacancy defects in 1T′-$MoTe_2$. (a) Atomic model of monolayer 1T′-$MoTe_2$ displaying the configurations of characteristic Te atoms. (b) Atomic-resolution ADF-STEM image of Pt_{Te} V_{Te}-$MoTe_2$ synthesized under the electrochemical exfoliation voltage of −4 V. (c) Schematic atomic model of the white box region from (b) illustrating the spatial distribution of Te vacancies and Pt anti-substitutions. Blue balls, Mo atoms; yellow balls, Te_1 atoms; light orange balls, Te_2 atoms; orange balls, Pt anti-substitutions; pink balls, Te vacancies. (d) Atomic-resolution ADF-STEM images showing the different coupled anti-substitution-vacancy structures of (i) $Pt_{Te_{22}}V_{Te_{11}}$, (ii) $Pt_{Te_{21}}V_{Te_{13}}$, (iii) $Pt_{Te_{21}}V_{Te_{12}}$, (iv) $Pt_{Te_{22}}V_{Te_{21}}$, (v) $Pt_{Te_{12}}V_{Te_{11}}$, with the corresponding atomic models, simulated images, and intensity line profiles displayed in sequence from the top to bottom panels, respectively. (e) Statistical counting of a variety of coupled anti-substitution-vacancy defects. (f) DFT-calculated formation energies of various coupled anti-substitution-vacancy defects as a function of Pt chemical potential. Scale bars: (b) 2 nm, (d) 0.2 nm.

foreign atomically dispersed atoms, we utilize Pt foil serving as the anode for electrochemical exfoliation.[40] Notably, ADF-STEM imaging together with EDS measurements confirm the presence of a large number of atomically dispersed Pt anti-substitutions (2.02%) in monolayer $MoTe_2$ (Figure 3a,b and Supporting Figure 6 and Supporting Table 2), denoted as Pt_{Te}-$MoTe_2$. Based on the Zernike polynomial clustering model analysis, five distinct Pt coordination structures are revealed (Figure 3c), including two anti-substitution sites where Pt substitutes Te sites (Pt_{Te_1} (Figure 3c(i)) and Pt_{Te_2} (Figure 3c(iv))), and three coupled $Pt_{Te_1}$and Pt_{Te_2} structures ($Pt_{Te_1}Pt_{Te_1}$ (Figure 3c(ii)), $Pt_{Te_1}Pt_{Te_2}$ (Figure 3c(iii)) and $Pt_{Te_2}Pt_{Te_2}$ (Figure 3c(v))). These configurations are corroborated by the consistency in the intensity line profiles between the experimental and corresponding simulated images. Statistical analysis of STEM images over areas larger than 10 × 10 nm based on the customized algorithm reveals that the density of Pt_{Te_1} is approximately one time larger than that of Pt_{Te_2} (Figure 3d) with a density of 0.3 nm^{-2}, and ∼50% Te_1 vacancies are occupied by Pt atoms. The formation energies of all Pt anti-substitutions are exclusively negative, indicating that they are all thermodynamically stable (Figure 3e). A relatively higher occurrence of Pt_{Te_1} is perhaps due to a higher initial density of in situ generated V_{Te_1} compared to that of V_{Te_2} during the electrochemical exfoliation. Furthermore, the preferred formation of Pt_{Te_1} as opposed to Pt_{Te_2} is presumably due to a large

https://doi.org/10.1021/jacs.5c00033
J. Am. Chem. Soc. 2025, 147, 9825−9835

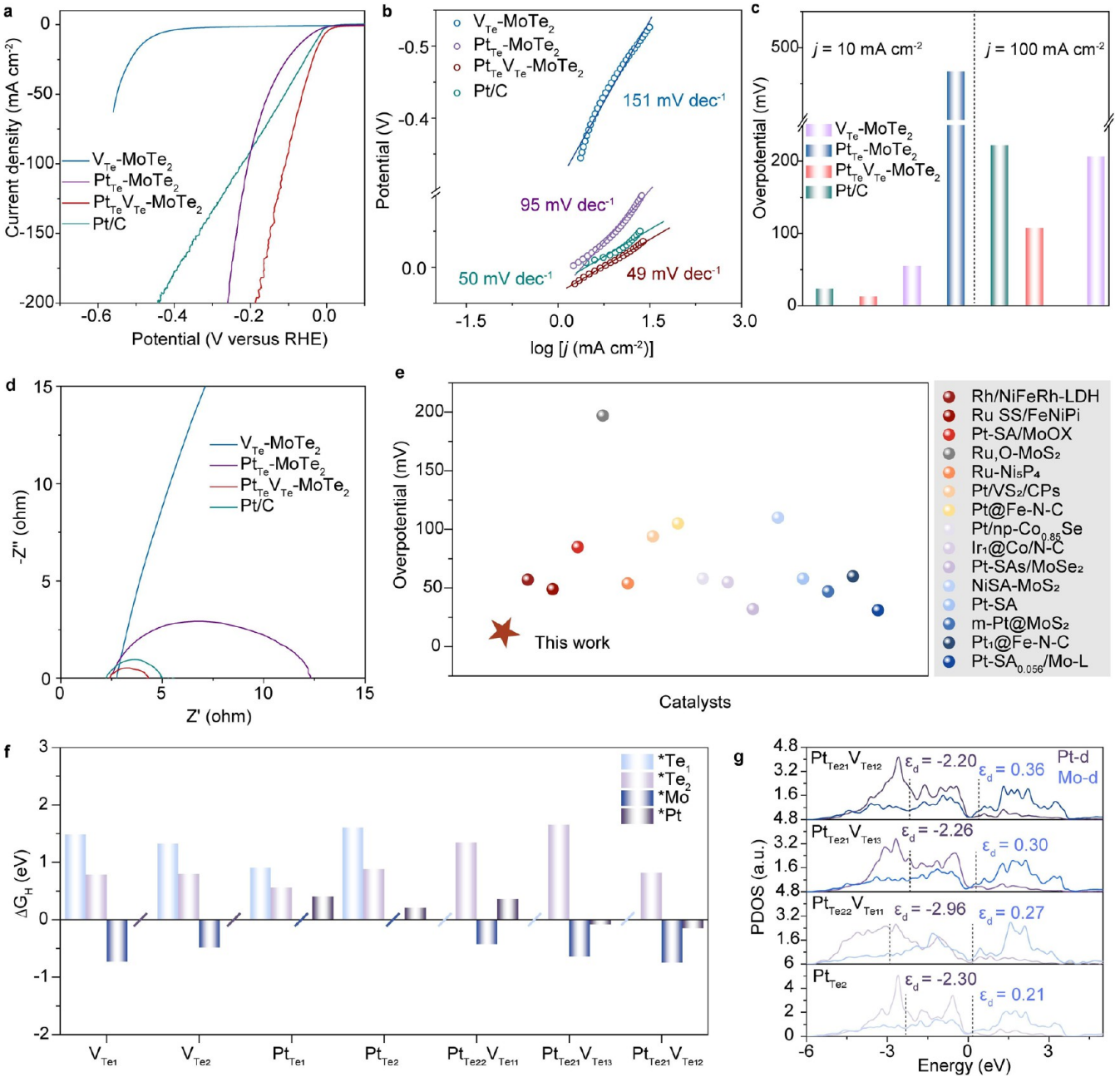

Figure 5. HER performance and DFT calculations. (a) Polarization curves of V_{Te}-MoTe$_2$, Pt_{Te}-MoTe$_2$, $Pt_{Te}V_{Te}$-MoTe$_2$, and commerical Pt/C for HER in 0.5 M H_2SO_4 at the scan rate of 5 mV s^{-1}. (b) Tafel plots. (c) Comparison for overpotentials of various samples at the current density of 10 and 100 mA cm^{-2}. (d) Electrochemical impedance spectroscopy (EIS) Nyquist plots. (e) Comparison for overpotential at 10 mA cm^{-2} with other single atomic catalysts. (f) Hydrogen adsorption free energy (ΔG_{H^*}) on different active sites in V_{Te_1}-MoTe$_2$, V_{Te_2}-MoTe$_2$, Pt_{Te_1}-MoTe$_2$, Pt_{Te_2}-MoTe$_2$, $Pt_{Te_{22}}V_{Te_{11}}$, $Pt_{Te_{21}}V_{Te_{13}}$, and $Pt_{Te_{21}}V_{Te_{12}}$. (g) Partial density of states (PDOS) of d-band of Pt anti-substitutions and Mo sites in Pt_{Te_2}-MoTe$_2$, $Pt_{Te_{22}}V_{Te_{11}}$, $Pt_{Te_{21}}V_{Te_{13}}$, and $Pt_{Te_{21}}V_{Te_{12}}$.

strain release along the Te_1 vacancies when forming Pt_{Te_1} (Supporting Figure 7).

We have demonstrated that the electrochemical exfoliation-induced leaching and deposition method is an effective approach for creating atomic and diatomic Pt anti-substitution in 1T′-MoTe$_2$. To raise the density of Pt anti-substitution and investigate the vacancy−anti-substitution coupling, we decreased the electrochemical exfoliation voltage to −4 V to create more abundant Te vacancies (Supporting Table 3). To precisely differentiate the structural characteristics of coupled Pt anti-substitutions and associated Te vacancy sites, six Te atoms surrounding a Mo atom are designated as Te_{11}, Te_{12}, Te_{13}, Te_{21}, Te_{22}, and Te_{23}, as illustrated in Figure 4a. ADF-STEM image with a relatively large field of view (Figure 4b) and atomic models obtained via feature representative clustering (FRC) (Figure 4c and Supporting Figure 8) confirm the coexistence of coupled Pt anti-substitutions and Te vacancies in 1T′-MoTe$_2$ synthesized. The versatile coupled vacancy−anti-substitution defects configurations are revealed by ADF-STEM imaging (Figure 4d), including Pt substituting the Te_{22} site with an adjacent Te_{11} vacancy ($Pt_{Te_{22}}V_{Te_{11}}$ (Figure

https://doi.org/10.1021/jacs.5c00033
J. Am. Chem. Soc. 2025, 147, 9825−9835

4d(i))), Pt at the Te_{21} site with a Te_{13} vacancy ($Pt_{Te_{21}}V_{Te_{13}}$ (Figure 4d(ii))), Pt at the Te_{21} site adjacent to a Te_{12} vacancy ($Pt_{Te_{21}}V_{Te_{12}}$ (Figure 4d(iii))), Pt at the Te_{22} site together with a neighboring Te_{21} vacancy ($Pt_{Te_{22}}V_{Te_{21}}$ (Figure 4d(iv))), and Pt at the Te_{12} site adjacent to a Te_{11} vacancy ($Pt_{Te_{12}}V_{Te_{11}}$ (Figure 4d(v))). The identification of these coupled defect structures is robustly justified by the quantitative intensity line profiles extracted from the experimental and simulated images. Statistically, the majority of Pt atoms substitute at Te_2 sites, with one Te_1 vacancy surrounding anti-substitution Pt_{Te_2} (Figure 4e), indicating that the anti-substitution Pt_{Te_2} lowers the formation energy of coupled vacancy complexes via strain releasing (Supporting Figure 9), which was further supported by the theoretical calculations (Figure 4f). Meanwhile, under high-energy electron bombardment, the positions of Pt and Te did not change significantly, indicating that the structure was thermodynamically stable, substituting the Te sites (Supporting Figure 10).

Electrocatalytic HER Performance and DFT Calculations. Substitutions and substitution-vacancy-coupled complexes could potentially enhance the catalytic properties,[41] particularly the anti-substitutions together with their complexes, due to drastically modified electronic and catalytic structures. To precisely validate the impact of Pt anti-substitutions, we systematically tested the HER performances of V_{Te}-$MoTe_2$, Pt_{Te}-$MoTe_2$, and $Pt_{Te}V_{Te}$-$MoTe_2$ catalysts in acidic electrolytes, respectively. As displayed in the linear sweep voltammetry (LSV) curves (Figure 5a), $Pt_{Te}V_{Te}$-$MoTe_2$ show a substantially larger geometric HER current density (J) than V_{Te}-$MoTe_2$ at the same overpotential resulting from the more exposed active sites of $MoTe_2$ after EELR process.[42] Interestingly, the HER activity is gradually enhanced from V_{Te}-$MoTe_2$ to Pt_{Te}-$MoTe_2$ because of the accelerated catalytic kinetics as shown in the corresponding Tafel slopes (Figure 5b).[43,44] The $Pt_{Te}V_{Te}$-$MoTe_2$ feature an exceptionally low HER overpotential (12.9 mV at η = 10 mA cm^{-2}; 107.6 mV cm^{-2} at η = 100 mA cm^{-2}, Figure 5c), superior to the state-of-the-art 20 wt % Pt/C catalyst (23.6 mV at η = 10 m Acm^{-2}; 221.9 mV at η = 100 mA cm^{-2}, Figure 5c). The derived electrochemical double layer capacitance (C_{dl}) and electrochemically active surface area (ECSA) were performed to get insights into the catalytic performance of the prepared material. Compared to commercial Pt/C, $Pt_{Te}V_{Te}$-$MoTe_2$ exhibits higher C_{dl} value, larger ECSA,[45,46] and larger intrinsic specific current (normalized to ECSA) (Supporting Figures 11 and 12).

Apart from the activity, catalytic stability is equally important in practical applications. Accelerated cyclic voltammetry (CV) test elucidates the robustness of $Pt_{Te}V_{Te}$-$MoTe_2$ in HER catalysis with virtually unchanged polarization curves even after 20,000 CV cycles (Supporting Figure 13). The durability of $Pt_{Te}V_{Te}$-$MoTe_2$ was also confirmed by the chronopotentiometry (CP) test. The overpotential (@10 mA cm^{-2}) exhibits negligible change during a 22-h CP test (Supporting Figure 14). The high HER activity of the $Pt_{Te}V_{Te}$-$MoTe_2$ can be further supported by the electrochemical impedance spectroscopy (EIS) results (Figure 5d), which display significantly reduced charge transfer resistance compared to the V_{Te}-$MoTe_2$.[47] The similar catalytic trend of $Pt_{Te}V_{Te}$-$MoTe_2$ for HER was also demonstrated in the acidic electrolyte, compared to the recently reported single-atom catalysts (Figure 5e and Supporting Table 4). Notably, $Pt_{Te}V_{Te}$-$MoTe_2$ displays the lowest overpotential, underscoring that the integration of the Pt anti-substitution with defects substantially enhances the hydrogen evolution performance. This phenomenon arises from the fact that the Pt anti-substitution resides on the surface, exhibiting a more pronounced interaction with surface anion vacancies and a shorter reaction pathway compared to metal atom substitution sites or adsorbed on the top sites.[27,48]

To shed light on the influence of ordered clustering of Te vacancies, Pt anti-substitutions, and Te vacancy and Pt anti-substitution coupled structures in atomically thin $MoTe_2$ on HER activity, a series of first-principles theoretical calculations were performed based on the first principal methods. An ideal HER catalyst should bind to hydrogen neither too strong nor too weak, giving rise to the hydrogen adsorption free energy (ΔG_{H^*}) close to zero.[49,50] The monolayer $MoTe_2$, containing a Te_1 or Te_2 vacancy, was constructed to model the different structures of V_{Te}-$MoTe_2$ (denoted as V_{Te_1}-$MoTe_2$ and V_{Te_2}-$MoTe_2$) (Supporting Figure 15). It can be observed that the ΔG_{H^*} of Mo sites for V_{Te}-$MoTe_2$ is lower than that of the Te sites. Specifically, the value of ΔG_{H^*} of the Mo site in V_{Te_2}-$MoTe_2$ is −0.49 eV, lower than those recorded at other sites in V_{Te}-$MoTe_2$ (Figure 5f). Monolayer $MoTe_2$, incorporating Pt substituting for a Te_1 or Te_2 atom, were synthesized to represent distinct configurations of Pt_{Te}-$MoTe_2$, denoted as Pt_{Te_1}-$MoTe_2$ and Pt_{Te_2}-$MoTe_2$, respectively (Supporting Figure 16). The ΔG_{H^*} values of the Pt anti-substitutions in $MoTe_2$ are consistently lower than those at Te sites. Specifically, the lower ΔG_{H^*} values of the Pt sites in Pt_{Te}-$MoTe_2$ are recorded at 0.41 and 0.21 eV (Figure 5f). In addition, we further analyzed the different active sites from V_{Te}-$MoTe_2$ and Pt_{Te}-$MoTe_2$ in $Pt_{Te}V_{Te}$-$MoTe_2$, and the results showed that Pt anti-substitution and Mo atoms are the optimal HER active centers (Figure 5f and Supporting Figure 17). Especially, in $Pt_{Te}V_{Te}$-$MoTe_2$, the ΔG_{H^*} values of Pt anti-substitution are −0.08 and −0.14 eV in $Pt_{Te_{21}}V_{Te_{13}}$ and $Pt_{Te_{21}}V_{Te_{12}}$, respectively, and the ΔG_{H^*} value of the Mo site is −0.43 eV in $Pt_{Te_{22}}V_{Te_{11}}$, lower than that of other active sites in V_{Te}-$MoTe_2$ and Pt_{Te}-$MoTe_2$. Therefore, the coupling effect of Pt anti-substitutions and Te vacancies increased the intrinsic activity and number of active sites (Supporting Figure 18).

To unveil the electronic structures of Pt anti-substitution and Te vacancy coupled structures, partial density of states (PDOS), and corresponding d-band center and charger density of Pt_{Te_2}-$MoTe_2$, $Pt_{Te_{22}}V_{Te_{11}}$, $Pt_{Te_{21}}V_{Te_{13}}$, and $Pt_{Te_{21}}V_{Te_{12}}$ structures were calculated. The PDOS results reveal a strong orbital overlap among Pt 5d and Mo 4d orbitals, confirming the strongly coupled interaction between the Pt and Mo atoms (Figure 5g). The Pt_{Te_2}-$MoTe_2$ structure is displayed for comparison of Pt anti-substitution and Te vacancy coupled structure configurations. The calculated Pt d-band center of the $Pt_{Te_{21}}V_{Te_{13}}$ (−2.26 eV) and $Pt_{Te_{21}}V_{Te_{12}}$ (−2.20 eV) displayed a significant upshift compared with that of the Pt_{Te_2}-$MoTe_2$ (−2.30 eV). However, the Mo d-band center of $Pt_{Te_{22}}V_{Te_{11}}$ (0.27 eV) is closest to the Fermi level, compared to $Pt_{Te_{21}}V_{Te_{13}}$ (0.30 eV) and $Pt_{Te_{21}}V_{Te_{12}}$ (0.36 eV) (Figure 5g). Correspondingly, the hydrogen adsorption energies of Pt anti-substitutions and adjacent Mo sites in $Pt_{Te_{22}}V_{Te_{11}}$, $Pt_{Te_{21}}V_{Te_{13}}$, and $Pt_{Te_{21}}V_{Te_{12}}$ simultaneously change, in line with the electronic structure

https://doi.org/10.1021/jacs.5c00033
J. Am. Chem. Soc. 2025, 147, 9825−9835

modulations (Figure 5f and Supporting Figures 17 and 19). Therefore, the Pt anti-substitution and Te vacancy coupled structures regulate the electronic structure and hydrogen adsorption energy. Structural distortion is often accompanied by the redistribution of the charge density. The introduction of Te vacancies leads to local lattice distortions and charge density redistributions, which will have a significant impact on catalytic activity.[51] Due to the diversity of Te vacancy and Pt anti-substitution structures, $Pt_{Te}V_{Te}$-$MoTe_2$ exhibits completely different and asymmetric charge density distribution (Supporting Figures 20 and 21). The red and blue regions refer to the charge accumulation and charge depletion regions, respectively. Apparently, the coupling between Te vacancy and Pt anti-substitution triggers substantial charge redistributions, resulting in charge transfer from Pt atoms to adjacent Mo atoms. Hence, the asymmetric charge density of Te defect atoms and neighboring Pt and Mo atoms have been effectively modulated, which promotes the activity of catalytic sites to a greater extent for the adsorption of H* (Figure 5f), leading to supreme catalytic efficiency.

CONCLUSIONS

In summary, Pt anti-substitution was atomically dispersed in monolayer $MoTe_2$ by a one-step electrochemical exfoliation. The atomic and electronic structures of Pt anti-substitution and Te defects were unveiled by ADF-STEM imaging and DFT calculations. STEM results confirmed the successful synthesis of atomically dispersed Pt anti-substitutions in monolayer $MoTe_2$, exhibiting diverse coordination structures. DFT calculations indicate that the resulting 1T′-$MoTe_2$ with Te vacancies exists in a metastable state, with Pt atoms stably anchored at Te sites to form Pt anti-substitutions. By modulating the exfoliation condition coupled Pt anti-substitution and Te vacancies were generated, leading to improved hydrogen evolution reaction due to negligible ΔG_{H^*}. Our results not only deepen our understanding of the new types of atomic defects, i.e., anti-substitutions, in two-dimensional (2D) materials but also advance an efficient and cost-effective defect engineering approach for optimizing 2D electrochemical catalysts at the atomic level.

MATERIALS AND METHODS

Synthesis of $MoTe_2$ Crystalline. 1T′-$MoTe_2$ crystals were fabricated by utilizing chemical vapor transport (CVT) with iodine serving as the transport agent. $MoTe_2$ powder was synthesized by annealing stoichiometrically mixed powders of molybdenum (99.999%, Sigma-Aldrich) and tellurium (99.9%, Sigma-Aldrich) at 750 °C for 72 h within an evacuated and sealed quartz ampule. $MoTe_2$ crystals were subsequently generated by encapsulating approximately 200 mg of the polycrystalline $MoTe_2$ powder along with a minor quantity of iodine (99.8%, 4 mg cm^{-3}, Sigma-Aldrich) in evacuated quartz ampules measuring 17 cm in length. These ampules were positioned within a furnace configured to maintain a temperature gradient, where the charge of $MoTe_2$ was held at 1000 °C, and the temperature at the distal end of the ampule approximated 950 °C. Following a growth period of 7 days, the ampule was rapidly quenched in ice water to preserve the 1T′ phase of $MoTe_2$.

Electrochemical Exfoliation. Electrochemical exfoliation of 1T′-$MoTe_2$ was conducted by using an electrochemical workstation (CHI760E) equipped with a two-electrode system. Bulk crystals were secured in a copper electrode clip serving as the cathode with a graphite rod acting as the counter electrode (refer to Figure 1a). An equal volume of 0.005 M tetrahexylammonium chloride (THA·Cl, Sigma-Aldrich) dissolved in acetonitrile (AN, Greagent) was employed as the electrolyte. To facilitate high-yield exfoliation of 1T′-$MoTe_2$ monolayers, a constant negative voltage was applied to promote homogeneous intercalation of ammonium cations into the vdW gaps of the $MoTe_2$ crystal, followed by gentle expansion and exfoliation. The exfoliated products were transferred to a centrifuge tube, and a well-dispersed ink solution was achieved after manual shaking followed by mild sonication. High-speed centrifugation at 10,000 rpm/s was employed to remove the electrolyte, and the residue was subsequently heated in a high vacuum annealing system to produce 1T′-$MoTe_2$ powder.

Synthesis of Pt_{Te}-$MoTe_2$ and $Pt_{Te}V_{Te}$-$MoTe_2$. In the electrochemical exfoliation process described above, the counter electrode is replaced by Pt foil. The applied voltage is −3 V for preparing Pt_{Te}-$MoTe_2$, and −4 V is used for $Pt_{Te}V_{Te}$-$MoTe_2$.

Characterization. SAED imaging was done by a JEOL-F200 operating at 200 kV. Aberration-corrected ADF-STEM images and EDS were obtained by a JEOL ARM200F operating at 80 kV. The ADF-STEM images were filtered by Gaussian filters, and the positions of atomic columns were located by finding the local maxima of the filtered series.

Atom Peak Finding. Feature point identification involves three steps: smoothing, maximum filtering, and locating the points. The first step, which is crucial for successful feature point extraction, is obtaining smooth versions of raw images. Depending on the image quality and conditions, different smoothing schemes are applied. For images with a high signal-to-noise ratio (SNR), Fourier space filtering is used to retain 10% of the lowest-frequency components. For low SNR images, a singular value decomposition (SVD)−based method is employed. Unless otherwise stated, we use the SVD-based method for the images in this work. The second step involves dilating the smoothed image using a local maximum filter. In the third step, feature points are identified where the input image matches the dilated version. This identification scheme might conservatively overestimate the number of feature points; these points can be further refined using the symmetry response of Zernike features or by selecting them in an FR clustering scheme. Notably, our Zernike polynomial (ZP) representation is more robust to position perturbation compared with principal component analysis (PCA). While ZPs show near-perfect tolerance within 4 pixels, we recommend enhancing the accuracy of feature point identification in extreme cases to improve overall performance in downstream analysis.[38]

Electrochemical Measurements. The electrocatalytic performance was evaluated using a three-electrode system with a CHI 760E electrochemical workstation. A graphite rod electrode served as the counter electrode, while a Hg/HgCl electrode acted as the reference electrode. The carbon cloth coated with catalyst ink served as the working electrode. The HER activity was assessed in 0.5 M N_2-saturated H_2SO_4 electrolyte through linear sweep voltammetry at a scan rate of 5 mV s^{-1}. All reported potentials were converted to reversible hydrogen electrode (RHE) potentials, and an *iR* correction was applied in all of the electrochemical measurements.

Computational Methods. We have employed the first-principles to perform spin-polarization DFT calculations within the generalized gradient approximation (GGA) using the Perdew−Burke−Ernzerhof (PBE)[52] formulation by the Vienna Ab initio Simulation Package (VASP).[53] We have chosen the projected augmented wave (PAW) potentials to describe the ionic cores and take valence electrons into account using a plane wave basis set with a kinetic energy cutoff of 500 eV.[54] Partial occupancies of the Kohn−Sham orbitals were allowed using the Gaussian smearing method and a width of 0.05 eV. The electronic energy was considered to be self-consistent when the energy change was smaller than 10^{-5} eV. A geometry optimization was considered to be convergent when the energy change was smaller than 0.05 eV $Å^{-1}$. The vacuum spacing in a direction perpendicular to the plane of the structure is 16 Å. The Brillouin zone integration is performed using 3 × 3 × 1 Monkhorst−Pack *k*-point sampling for a structure. The long-range dispersion interaction was described by the DFT-D3 method. Finally, the adsorption energies (E_{ads}) were calculated as $E_{ads} = E_{ad/sub} - E_{ad} - E_{sub}$, where $E_{ad/sub}$, E_{ad}, and E_{sub} are the total energies of the optimized adsorbate/substrate system, the

https://doi.org/10.1021/jacs.5c00033
J. Am. Chem. Soc. 2025, 147, 9825−9835

adsorbate in the structure, and the clean substrate, respectively. The free energy was calculated using eq 1

$$G = E + \mathrm{ZPE} - \mathrm{TS} \quad (1)$$

where G, E, ZPE, and TS are the free energy, total energy from DFT calculations, zero-point energy, and entropic contributions, respectively.

The Gibbs free energy of the reaction steps can be calculated by the following formula in eq 2

$$* + \mathrm{H}^+ + \mathrm{e}^- = \mathrm{H}^* \quad (2)$$

The formation energy of different defects was calculated by the following eq 3

$$E_f = E^t(\mathrm{def}) - E^t(\mathrm{ideal}) + \sum N\mu \quad (3)$$

where E^t (def) and E^t (def) represent the total energies of defective and pristine $MoTe_2$, respectively, and μ and N represent the chemical potentials of Te or Pt atom in $MoTe_2$ and the defects number, respectively.

■ ASSOCIATED CONTENT

Data Availability Statement

The data that support the findings of this study are available from the corresponding author upon request.

Supporting Information

The Supporting Information is available free of charge at https://pubs.acs.org/doi/10.1021/jacs.5c00033.

SAED and STEM images; EDS mapping; atomic models; structural distortions; CV curves; ECSA; LSV curves; CP; ICOHP; charge density; EDS tables; and comparison of HER performances for $Pt_{Te}V_{Te}$-$MoTe_2$ and Pt_{Te}-$MoTe_2$ with the recently reported single atomic catalysts (PDF)

■ AUTHOR INFORMATION

Corresponding Author

Xiaoxu Zhao − *School of Materials Science and Engineering, Peking University, Beijing 100871, China;* orcid.org/0000-0001-9746-3770; Email: xiaoxuzhao@pku.edu.cn

Authors

Jun Zhao − *School of Materials Science and Engineering, Peking University, Beijing 100871, China;* orcid.org/0009-0007-3151-4847

Xiaocang Han − *School of Materials Science and Engineering, Peking University, Beijing 100871, China*

Junxian Li − *School of Materials Science and Engineering, Peking University, Beijing 100871, China*

Ziyi Han − *School of Materials Science and Engineering, Peking University, Beijing 100871, China*

Complete contact information is available at: https://pubs.acs.org/10.1021/jacs.5c00033

Author Contributions

†J.Z., X.H., and J.L. contributed equally to this work. X.Z. conceived and supervised the project. J.Z. designed experiments, tested electrochemical performance, analyzed the data, and wrote the manuscript. X.H. performed STEM characterizations and revised the manuscript. J.L. performed atom peak finding. Z.H. helped with the data analysis.

Notes

The authors declare no competing financial interest.

■ ACKNOWLEDGMENTS

This work was financially supported by the National Key R&D Program of China (2024YFE0109200, 2024YFA1410000), the Beijing Natural Science Foundation (JQ24010, Z220020), the National Natural Science Foundation of China (Grant No. 22494643, 52273279), the open research fund of Songshan Lake Materials Laboratory (Grant No. 2023SLABFN26), the Young Scientists Fund of the National Natural Science Foundation of China (52403289), the Postdoctoral Fellowship Program of China Postdoctoral Science Foundation (Grant No. GZC20230039), and the China Postdoctoral Science Foundation (Grant Nos. 2023M740032, 2024M750097). The authors acknowledge Electron Microscopy Laboratory of Peking University, China, for the use of Cs-corrected JEOL ARM200F transmission electron microscopy. They thank Materials Processing and Analysis Center, Peking University, for assistance with SAED and STEM characterization.

■ REFERENCES

(1) Zheng, Y.; Slade, T. J.; Hu, L.; Tan, X. Y.; Luo, Y.; Luo, Z.-Z.; Xu, J.; Yan, Q.; Kanatzidis, M. G. Defect engineering in thermoelectric materials: what have we learned? *Chem. Soc. Rev.* **2021**, *50*, 9022−9054.

(2) Weitering, H. H.; Carpinelli, J. M.; Melechko, A. V.; Zhang, J.; Bartkowiak, M.; Plummer, E. W. Defect-mediated condensation of a charge density wave. *Science* **1999**, *285*, 2107−2110.

(3) Liu, F.; Fan, Z. Defect engineering of two-dimensional materials for advanced energy conversion and storage. *Chem. Soc. Rev.* **2023**, *52*, 1723−1772.

(4) Suh, J.; Tan, T. L.; Zhao, W.; Park, J.; Lin, D.-Y.; Park, T.-E.; Kim, J.; Jin, C.; Saigal, N.; Ghosh, S.; Wong, Z. M.; Chen, Y.; Wang, F.; Walukiewicz, W.; Eda, G.; Wu, J. Reconfiguring crystal and electronic structures of MoS_2 by substitutional doping. *Nat. Commun.* **2018**, *9*, No. 199.

(5) Tian, X.; Kim, D. S.; Yang, S.; Ciccarino, C. J.; Gong, Y.; Yang, Y.; Yang, Y.; Duschatko, B.; Yuan, Y.; Ajayan, P. M.; Idrobo, J. C.; Narang, P.; Miao, J. Correlating the three-dimensional atomic defects and electronic properties of two-dimensional transition metal dichalcogenides. *Nat. Mater.* **2020**, *19*, 867−873.

(6) Duan, X.; Zhang, H. Introduction: Two-Dimensional Layered Transition Metal Dichalcogenides. *Chem. Rev.* **2024**, *124*, 10619−10622.

(7) Han, X.; Niu, M.; Luo, Y.; Li, R.; Dan, J.; Hong, Y.; Wu, X.; Trukhanov, A. V.; Ji, W.; Zhou, J.; Qiao, J.; Wang, Y.; Zhang, J.; Zhao, X. Atomically engineering metal vacancies in monolayer transition metal dichalcogenides. *Nat. Synth.* **2024**, *3*, 586−594.

(8) Hus, S. M.; Ge, R.; Chen, P.-A.; Liang, L.; Donnelly, G. E.; Ko, W.; Huang, F.; Chiang, M.-H.; Li, A.-P.; Akinwande, D. Observation of single-defect memristor in an MoS_2 atomic sheet. *Nat. Nanotechnol.* **2021**, *16*, 58−62.

(9) Zheng, Y. J.; Chen, Y.; Huang, Y. L.; Gogoi, P. K.; Li, M.-Y.; Li, L.-J.; Trevisanutto, P. E.; Wang, Q.; Pennycook, S. J.; Wee, A. T. S.; Quek, S. Y. Point Defects and Localized Excitons in 2D WSe_2. *ACS Nano* **2019**, *13*, 6050−6059.

(10) Moody, G.; Tran, K.; Lu, X.; Autry, T.; Fraser, J. M.; Mirin, R. P.; Yang, L.; Li, X.; Silverman, K. L. Microsecond Valley Lifetime of Defect-Bound Excitons in Monolayer WSe_2. *Phys. Rev. Lett.* **2018**, *121*, No. 057403.

(11) Liu, C.; Chen, H.; Wang, S.; Liu, Q.; Jiang, Y.-G.; Zhang, D. W.; Liu, M.; Zhou, P. Two-dimensional materials for next-generation computing technologies. *Nat. Nanotechnol.* **2020**, *15*, 545−557.

(12) Lin, Y.-C.; Dumcencon, D. O.; Huang, Y.-S.; Suenaga, K. Atomic mechanism of the semiconducting-to-metallic phase transition in single-layered MoS_2. *Nat. Nanotechnol.* **2014**, *9*, 391−396.

(13) Avsar, A.; Ciarrocchi, A.; Pizzochero, M.; Unuchek, D.; Yazyev, O. V.; Kis, A. Defect induced, layer-modulated magnetism in ultrathin metallic $PtSe_2$. *Nat. Nanotechnol.* **2019**, *14*, 674−678.

(14) Chua, R.; Yang, J.; He, X.; Yu, X.; Yu, W.; Bussolotti, F.; Wong, P. K. J.; Loh, K. P.; Breese, M. B. H.; Goh, K. E. J.; Huang, Y. L.; Wee, A. T. S. Can Reconstructed Se-Deficient Line Defects in Monolayer VSe_2 Induce Magnetism? *Adv. Mater.* **2020**, *32*, No. 2000693.
(15) Liang, Q.; Zhang, Q.; Zhao, X.; Liu, M.; Wee, A. T. S. Defect Engineering of Two-Dimensional Transition-Metal Dichalcogenides: Applications, Challenges, and Opportunities. *ACS Nano* **2021**, *15*, 2165−2181.
(16) Peng, H.; Liu, T.; Zhao, Y.; Li, L.; Du, P.; Li, H.; Yan, F.; Zhai, T. Ultrahigh Responsivity and Robust Semiconducting Fiber Enabled by Molecular Soldering-Governed Defect Engineering for Smart Textile Optoelectronics. *Adv. Mater.* **2024**, *36*, No. 2406353.
(17) Horzum, S.; Çakir, D.; Suh, J.; Tongay, S.; Huang, Y. S.; Ho, C. H.; Wu, J.; Sahin, H.; Peeters, F. M. Formation and stability of point defects in monolayer rhenium disulfide. *Phys. Rev. B* **2014**, *89*, No. 155433.
(18) Greben, K.; Arora, S.; Harats, M. G.; Bolotin, K. I. Intrinsic and Extrinsic Defect-Related Excitons in TMDCs. *Nano Lett.* **2020**, *20*, 2544−2550.
(19) Tsai, J.-Y.; Pan, J.; Lin, H.; Bansil, A.; Yan, Q. Antisite defect qubits in monolayer transition metal dichalcogenides. *Nat. Commun.* **2022**, *13*, No. 492.
(20) Förster, A.; Gemming, S.; Seifert, G.; Tománek, D. Chemical and Electronic Repair Mechanism of Defects in MoS_2 Monolayers. *ACS Nano* **2017**, *11*, 9989−9996.
(21) Li, X.; Fang, Y.; Wang, J.; Fang, H.; Xi, S.; Zhao, X.; Xu, D.; Xu, H.; Yu, W.; Hai, X.; Chen, C.; Yao, C.; Tao, H. B.; Howe, A. G. R.; Pennycook, S. J.; Liu, B.; Lu, J.; Su, C. Ordered clustering of single atomic Te vacancies in atomically thin $PtTe_2$ promotes hydrogen evolution catalysis. *Nat. Commun.* **2021**, *12*, No. 2351.
(22) Mitterreiter, E.; Schuler, B.; Micevic, A.; Hernangómez-Pérez, D.; Barthelmi, K.; Cochrane, K. A.; Kiemle, J.; Sigger, F.; Klein, J.; Wong, E.; Barnard, E. S.; Watanabe, K.; Taniguchi, T.; Lorke, M.; Jahnke, F.; Finley, J. J.; Schwartzberg, A. M.; Qiu, D. Y.; Refaely-Abramson, S.; Holleitner, A. W.; Weber-Bargioni, A.; Kastl, C. The role of chalcogen vacancies for atomic defect emission in MoS_2. *Nat. Commun.* **2021**, *12*, No. 3822.
(23) Shen, P.-C.; Lin, Y.; Su, C.; McGahan, C.; Lu, A.-Y.; Ji, X.; Wang, X.; Wang, H.; Mao, N.; Guo, Y.; Park, J.-H.; Wang, Y.; Tisdale, W.; Li, J.; Ling, X.; Aidala, K. E.; Palacios, T.; Kong, J. Healing of donor defect states in monolayer molybdenum disulfide using oxygen-incorporated chemical vapour deposition. *Nat. Electron.* **2022**, *5*, 28−36.
(24) Barja, S.; Refaely-Abramson, S.; Schuler, B.; Qiu, D. Y.; Pulkin, A.; Wickenburg, S.; Ryu, H.; Ugeda, M. M.; Kastl, C.; Chen, C.; Hwang, C.; Schwartzberg, A.; Aloni, S.; Mo, S. K.; Ogletree, D. F.; Crommie, M. F.; Yazyev, O. V.; Louie, S. G.; Neaton, J. B.; Weber-Bargioni, A. Identifying substitutional oxygen as a prolific point defect in monolayer transition metal dichalcogenides. *Nat. Commun.* **2019**, *10*, No. 3382.
(25) Hong, J.; Hu, Z.; Probert, M.; Li, K.; Lv, D.; Yang, X.; Gu, L.; Mao, N.; Feng, Q.; Xie, L.; Zhang, J.; Wu, D.; Zhang, Z.; Jin, C.; Ji, W.; Zhang, X.; Yuan, J.; Zhang, Z. Exploring atomic defects in molybdenum disulphide monolayers. *Nat. Commun.* **2015**, *6*, No. 6293.
(26) Yang, S.-Z.; Gong, Y.; Manchanda, P.; Zhang, Y.-Y.; Ye, G.; Chen, S.; Song, L.; Pantelides, S. T.; Ajayan, P. M.; Chisholm, M. F.; Zhou, W. Rhenium-Doped and Stabilized MoS_2 Atomic Layers with Basal-Plane Catalytic Activity. *Adv. Mater.* **2018**, *30*, No. 1803477.
(27) Shi, Z.; Zhang, X.; Lin, X.; Liu, G.; Ling, C.; Xi, S.; Chen, B.; Ge, Y.; Tan, C.; Lai, Z.; Huang, Z.; Ruan, X.; Zhai, L.; Li, L.; Li, Z.; Wang, X.; Nam, G.-H.; Liu, J.; He, Q.; Guan, Z.; Wang, J.; Lee, C.-S.; Kucernak, A. R. J.; Zhang, H. Phase-dependent growth of Pt on MoS_2 for highly efficient H_2 evolution. *Nature* **2023**, *621*, 300.
(28) Deng, J.; Li, H.; Xiao, J.; Tu, Y.; Deng, D.; Yang, H.; Tian, H.; Li, J.; Ren, P.; Bao, X. Triggering the electrocatalytic hydrogen evolution activity of the inert two-dimensional MoS_2 surface *via* single-atom metal doping. *Energy Environ. Sci.* **2015**, *8*, 1594−1601.
(29) Nipane, A.; Karmakar, D.; Kaushik, N.; Karande, S.; Lodha, S. Few-Layer MoS_2 *p*-Type Devices Enabled by Selective Doping Using Low Energy Phosphorus Implantation. *ACS Nano* **2016**, *10*, 2128−2137.
(30) Mattila, T.; Seitsonen, A. P.; Nieminen, R. M. Large atomic displacements associated with the nitrogen antisite in GaN. *Phys. Rev. B* **1996**, *54*, 1474−1477.
(31) Ning, S.; Kumar, A.; Klyukin, K.; Cho, E.; Kim, J. H.; Su, T.; Kim, H.-S.; LeBeau, J. M.; Yildiz, B.; Ross, C. A. An antisite defect mechanism for room temperature ferroelectricity in orthoferrites. *Nat. Commun.* **2021**, *12*, No. 4298.
(32) Zhao, X.; He, D.; Xia, B. Y.; Sun, Y.; You, B. Ambient Electrosynthesis toward Single-Atom Sites for Electrocatalytic Green Hydrogen Cycling. *Adv. Mater.* **2023**, *35*, No. 2210703.
(33) Yin, Y.; Han, J.; Zhang, Y.; Zhang, X.; Xu, P.; Yuan, Q.; Samad, L.; Wang, X.; Wang, Y.; Zhang, Z.; Zhang, P.; Cao, X.; Song, B.; Jin, S. Contributions of Phase, Sulfur Vacancies, and Edges to the Hydrogen Evolution Reaction Catalytic Activity of Porous Molybdenum Disulfide Nanosheets. *J. Am. Chem. Soc.* **2016**, *138*, 7965−7972.
(34) Gao, Y.; Liu, B.; Wang, D. Microenvironment Engineering of Single/Dual-Atom Catalysts for Electrocatalytic Application. *Adv. Mater.* **2023**, *35*, No. 2209654.
(35) Wang, S.; Xue, J.; Xu, D.; He, J.; Dai, Y.; Xia, T.; Huang, Y.; He, Q.; Duan, X.; Lin, Z. Electrochemical molecular intercalation and exfoliation of solution-processable two-dimensional crystals. *Nat. Protoc.* **2023**, *18*, 2814−2837.
(36) Li, J.; Song, P.; Zhao, J.; Vaklinova, K.; Zhao, X.; Li, Z.; Qiu, Z.; Wang, Z.; Lin, L.; Zhao, M.; Herng, T. S.; Zuo, Y.; Jonhson, W.; Yu, W.; Hai, X.; Lyu, P.; Xu, H.; Yang, H.; Chen, C.; Pennycook, S. J.; Ding, J.; Teng, J.; Neto, A. H. C.; Novoselov, K. S.; Lu, J. Printable two-dimensional superconducting monolayers. *Nat. Mater.* **2021**, *20*, 181−187.
(37) Zhang, S.; Li, H.; Wang, L.; Liu, J.; Liang, G.; Davey, K.; Ran, J.; Qiao, S.-Z. Boosted Photoreforming of Plastic Waste via Defect-Rich $NiPS_3$ Nanosheets. *J. Am. Chem. Soc.* **2023**, *145*, 6410−6419.
(38) Dan, J.; Zhao, X.; Ning, S.; Lu, J.; Loh, K. P.; He, Q.; Loh, N. D.; Pennycook, S. J. Learning motifs and their hierarchies in atomic resolution microscopy. *Sci. Adv.* **2022**, *8*, No. eabk1005.
(39) Lin, J.; Zhou, J.; Zuluaga, S.; Yu, P.; Gu, M.; Liu, Z.; Pantelides, S. T.; Suenaga, K. Anisotropic Ordering in 1T′ Molybdenum and Tungsten Ditelluride Layers Alloyed with Sulfur and Selenium. *ACS Nano* **2018**, *12*, 894−901.
(40) Zhang, L.; Han, L.; Liu, H.; Liu, X.; Luo, J. Potential-Cycling Synthesis of Single Platinum Atoms for Efficient Hydrogen Evolution in Neutral Media. *Angew. Chem., Int. Ed.* **2017**, *56*, 13694−13698.
(41) Zhai, P.; Xia, M.; Wu, Y.; Zhang, G.; Gao, J.; Zhang, B.; Cao, S.; Zhang, Y.; Li, Z.; Fan, Z.; Wang, C.; Zhang, X.; Miller, J. T.; Sun, L.; Hou, J. Engineering single-atomic ruthenium catalytic sites on defective nickel-iron layered double hydroxide for overall water splitting. *Nat. Commun.* **2021**, *12*, No. 4587.
(42) Wang, X.; Ding, J.; Song, W.; Yang, X.; Zhang, T.; Huang, Z.; Wang, H.; Han, X.; Hu, W. Cation Vacancy Clusters in $Ti_3C_2T_x$ MXene Induce Ultra-Strong Interaction with Noble Metal Clusters for Efficient Electrocatalytic Hydrogen Evolution. *Adv. Energy Mater.* **2023**, *13*, No. 2300148.
(43) Xu, J.; Xue, X.-X.; Shao, G.; Jing, C.; Dai, S.; He, K.; Jia, P.; Wang, S.; Yuan, Y.; Luo, J.; Luo, J.; Lu, J. Atomic-level polarization in electric fields of defects for electrocatalysis. *Nat. Commun.* **2023**, *14*, No. 7849.
(44) Han, C.; Zhang, S.; Zhang, H.; Dong, Y.; Yao, P.; Du, Y.; Song, P.; Gong, X.; Xu, W. Metal-support interaction in single-atom electrocatalysts: A perspective of metal oxide supports. *eScience* **2024**, *4*, No. 100269.
(45) McCrory, C. C. L.; Jung, S.; Peters, J. C.; Jaramillo, T. F. Benchmarking Heterogeneous Electrocatalysts for the Oxygen Evolution Reaction. *J. Am. Chem. Soc.* **2013**, *135*, 16977−16987.
(46) Zhang, Y.; Guo, P.; Guo, S.; Xin, X.; Wang, Y.; Huang, W.; Wang, M.; Yang, B.; Sobrido, A. J.; Ghasemi, J. B.; Yu, J.; Li, X. Gradient Heating Epitaxial Growth Gives Well Lattice-Matched

https://doi.org/10.1021/jacs.5c00033
J. Am. Chem. Soc. 2025, 147, 9825−9835

Mo_2C-Mo_2N Heterointerfaces that Boost Both Electrocatalytic Hydrogen Evolution and Water Vapor Splitting. *Angew. Chem., Int. Ed.* **2022**, *61*, No. e202209703.
(47) Shao, W.; Xing, Z.; Xu, X.; Ye, D.; Yan, R.; Ma, T.; Wang, Y.; Zeng, Z.; Yin, B.; Cheng, C.; Li, S. Bioinspired Proton Pump on Ferroelectric HfO_2-Coupled Ir Catalysts with Bidirectional Hydrogen Spillover for pH-Universal and Superior Hydrogen Production. *J. Am. Chem. Soc.* **2024**, *146*, 27486−27498.
(48) Wei, J.; Xiao, K.; Chen, Y.; Guo, X.-P.; Huang, B.; Liu, Z.-Q. *In situ* precise anchoring of Pt single atoms in spinel Mn_3O_4 for a highly efficient hydrogen evolution reaction. *Energy Environ. Sci.* **2022**, *15*, 4592−4600.
(49) Shen, F.; Zhang, Z.; Wang, Z.; Ren, H.; Liang, X.; Cai, Z.; Yang, S.; Sun, G.; Cao, Y.; Yang, X.; Hu, M.; Hao, Z.; Zhou, K. Oxophilic Ce single atoms-triggered active sites reverse for superior alkaline hydrogen evolution. *Nat. Commun.* **2024**, *15*, No. 448.
(50) Li, Z.; Fu, J.-Y.; Feng, Y.; Dong, C.-K.; Liu, H.; Du, X.-W. A silver catalyst activated by stacking faults for the hydrogen evolution reaction. *Nat. Catal.* **2019**, *2*, 1107−1114.
(51) Li, D.; Wang, B.; Long, X.; Xu, W.; Xia, Y.; Yang, D.; Yao, X. Controlled Asymmetric Charge Distribution of Active Centers in Conjugated Polymers for Oxygen Reduction. *Angew. Chem., Int. Ed.* **2021**, *60*, 26483−26488.
(52) Perdew, J. P.; Burke, K.; Ernzerhof, M. Generalized gradient approximation made simple. *Phys. Rev. Lett.* **1996**, *77*, 3865−3868.
(53) Kresse, G.; Furthmuller, J. Efficient iterative schemes for ab initio total-energy calculations using a plane-wave basis set. *Phys. Rev. B* **1996**, *54*, 11169−11186.
(54) Blöchl, P. E. Projector augmented-wave method. *Phys. Rev. B* **1994**, *50*, 17953−17979.

https://doi.org/10.1021/jacs.5c00033
J. Am. Chem. Soc. 2025, 147, 9825−9835